Numerical study of HCl and SO_2 impact on potassium emissions in pulverized-biomass combustion

Kaidi Wan[1], Zhihua Wang[2,*], Jun Xia[3,*], Luc Vervisch[1], Pascale Domingo[1], Yu Lv[4], Yingzu Liu[2], Yong He[2], Kefa Cen[2]

1. CORIA – CNRS, Normandie Université,
INSA de Rouen, 76800 Saint-Etienne-du-Rouvray, France

2. State Key Laboratory of Clean Energy Utilization,
Zhejiang University, Hangzhou 310027, China

3. Department of Mechanical and Aerospace Engineering & Institute of Energy Futures,
Brunel University London, Uxbridge UB8 3PH, UK

4. Department of Aerospace Engineering, Mississippi State University,
Mississippi State, MS 39762, USA

* Corresponding authors: wangzh@zju.edu.cn (Zhihua Wang); jun.xia@brunel.ac.uk (Jun Xia).

Abstract

The potassium vapor released during the combustion of biomass are known to result in serious ash deposition, fouling and corrosion issues of biomass furnaces. To develop potassium control technologies to mitigate these issues and achieve clean utilization of biomass fuel, a better understanding of the fundamental formation and transformation mechanisms of potassium in biomass combustion is essentially required. In the present study, potassium emissions during pulverized-biomass combustion, for the first time, have been simulated in both one-dimensional (1D) premixed/diffusion flames of the biomass volatile and an early-stage two-dimensional (2D) pulverized-biomass flame. The properties of corn straw are used. The volatile-gas combustion is described by the DRM22 skeletal mechanism, while the homogeneous reaction of potassium species is modeled using a detailed mechanism encompassing the elements K, C, H, O, Cl and S. The initial species of K, Cl and S in the volatile gas is set to be KOH, HCl and SO_2, respectively. The transformation characteristics of the potassium species are numerically investigated in both the 1D and 2D flames. Results show that KOH is the most significant potassium product under fuel-lean, stoichiometric and fuel-rich conditions, while the productions of sulfurous and chloric potassium species are secondary. Parametric studies with HCl, SO_2 or both species replaced with N_2 in volatile gas are then performed to study their impacts on potassium emission characteristics in both the 1D and 2D flames. The results indicate that HCl has a stronger ability to react with potassium species than SO_2.

Keywords: Pulverized-biomass combustion; Emission; Potassium chemistry; Alkali metal; HCl; SO_2

1. Introduction

As a renewable fuel source, biomass resources have been utilized to supply 10–15% of the worldwide energy consumption [1], especially with an increasing application in the production of thermal power. However, advanced biomass utilization is significantly limited by severe ash formation and deposition problems resulting from alkali metal issues [2]. Potassium (K) is usually rich in biomass, since it is an important element for plants. The potassium vapor released during the combustion of biomass is easy to condense on heat transfer surfaces and form an initial sticky layer, which then captures fly ash and therefore results in rapid ash deposition [3, 4]. In addition, potassium also reacts with chlorine and sulfur species to form complex compound, which leads to serious fouling and corrosion issues [5, 6]. Thus, understanding the fundamental formation and transformation mechanisms of potassium in biomass combustion is essential for the development of potassium control technologies and a better utilization of this renewable fuel [7-9].

Experimental research on the release and reacting dynamics of potassium evolves from offline sampling techniques to online measurement methods using laser diagnostics [2, 10-12]. Non-intrusive, time-resolved laser techniques, e.g., tunable diode laser absorption spectroscopy

(TDLAS) [13], collinear photo-fragmentation atomic absorption spectroscopy (CPFAAS) [14] and laser induced fragmentation fluorescence (ELIF) [15], can directly capture the dynamic release process of potassium during biomass combustion. In our recent study [16], the release of atomic and elemental potassium from a burning biomass pellet has been quantitatively measured via planar laser-induced fluorescence (PLIF) and multi-point laser-induced breakdown spectroscopy (LIBS) methods.

On the modeling side, Zhang et al. [17] proposed an one-step Arrhenius potassium release model during the combustion of a pinewood pellet. In our recent work [16], a two-step model was developed to describe the potassium release during both the pyrolysis and char burnout stages of two biomass samples, based on simultaneous measurements of the pellet-surface temperature, pellet diameter and potassium release of a burning biomass pellet. Since the pellet diameter and burnout time of biomass in these studies are on the same order of magnitude as in a typical circulating fluidized bed (CFB) boiler, these potassium release models are suitable for CFB combustion [18]. Potassium release models for pulverized-biomass combustion are still required to be developed.

Considering the post-release homogeneous reactions of alkali species, it has been found that the main alkali species are atomic K/Na, KOH/NaOH and KCl/NaCl in chemical equilibrium of post-combustion gases [19], which can be well predicted by thermodynamic equilibrium calculation, e.g., [18-20]. A detailed chemical reaction mechanism for alkali species has been proposed by Glarborg and Marshall [21], and validated with experimental data on sulfation of potassium chlorides. However, the numerical investigation on reaction dynamics of alkali species in turbulent reacting flows is still quite limited. Most of the relevant research employs Reynolds-averaged Navier-Stokes (RANS) simulation (e.g. [22, 23]) with simplified alkali reaction mechanisms to study the response of potassium in biomass combustion.

With the rapid increase of computing capacity in recent years, computational fluid dynamics (CFD) approaches for multi-phase flows are evolving towards high-fidelity methods, i.e., direct numerical simulation (DNS, e.g., [24-26]) and large-eddy simulation (LES, e.g. [27-34]). The two high-fidelity methods have shown advantages over RANS on the prediction of local gas temperature and species distributions. Our previous work [26, 34] on pulverized-coal combustion demonstrated that DNS and LES can provide detailed physical insights into complex multi-phase reacting flow dynamics and the homogeneous evolution of alkali species.

In sum, the reaction dynamics of potassium species in pulverized-biomass combustion have not been fully revealed by previous studies. In the present work, the responses of potassium species to one-dimensional (1D) premixed/diffusion flames of biomass volatile are firstly investigated. Then, the transformation dynamics of potassium species in a two-dimensional (2D) early-stage pulverized-biomass flame are numerically studied, excluding char combustion. Information about the major potassium product under various conditions and the comparison between the impacts of HCl and SO_2 on potassium conversion are revealed, which could potentially benefit the biomass combustion community. The full detailed potassium mechanism including the elements K, C, H, O, S and Cl proposed by Glarborg and Marshall [21] is utilized to model the potassium reactions during the simulation. It should be noted that Glarborg and Marshall [21] have carefully validated their detailed potassium mechanism against the experimental results of the homogeneous sulfation of potassium chloride at combustion conditions. The readers might notice that there exists a newer version of potassium mechanism by Hindiyarti et al. [35], which includes additional sulfation pathways of potassium to mainly improve the prediction of the mechanism at lower temperatures

[36]. However, since the present study focus on the potassium transformation under combustion conditions, thus at rather high temperature levels, the original version of the mechanism [21] is used to save the computational cost.

2. One-dimensional premixed/diffusion flames of biomass volatile

The reaction dynamics of potassium species in 1D premixed/diffusion flames of biomass volatile are studied. The volatile is released from corn straw [16], for which the chemical analysis data is shown in Table 1. The combustion of biomass volatile is modeled by the previously validated DRM22 skeletal mechanism involving 22 chemical species and 104 elementary reactions, which is proposed by Kazakov and Frenklach [37]. The bio-chemical percolation devolatilization (bio-CPD) model [38-40] is used to preliminary obtain the compositions of the volatile fuels and in which the Tar species is replaced by C_2H_2 [32]. Then the obtained compositions are adjusted to fulfill the elemental mass conservation and the lower heating value of the corn straw, as in [30, 33, 34]. The final volatile compositions used in the present study is shown in Table 2.

Table 1. Chemical analyses of corn straw.

Proximate analysis (wt%)				*Ultimate analysis (wt%)*				
M_{ad}	A_{ad}	V_{ad}	FC_{ad}	C_{daf}	H_{daf}	N_{daf}	S_{daf}	O_{daf}
11.6	7.9	64.2	16.3	43.9	4.5	1.8	0.4	49.3
Ash analysis (wt%)							Cl_{ad}	K_{ad}
SiO_2	Al_2O_3	Fe_2O_3	CaO	MgO	K_2O	Na_2O	*(mg/g)*	*(mg/g)*
47.52	5.64	1.04	4.51	12.6	7.87	1.97	1.34	13.1

Table 2. Modeled volatile-gas compositions of corn straw.

Hydrocarbon volatile compositions (mass fractions)					
CH_4	C_2H_2	CO	H_2	CO_2	H_2O
0.0322	0.1805	0.2536	0.0215	0.1853	0.3024
Non-hydrocarbon volatile compositions (mass fractions)					
KOH	HCl	SO_2			
0.0147	0.0018	0.0080			

Similar as previous studies on sodium emissions in coal combustion [41], KOH is set as the initial species of K, while HCl and SO_2 are set as the initial species of Cl and S, respectively. According to our previous experimental data [16], the percentage of potassium which is releasable during the biomass pyrolysis stage is set to 58.1%. Since the release of chlorine and sulfur has not been measured, their releasable proportions during the pyrolysis are both set to 87.3%, the volatile yields ratio predicted by the bio-CPD model [38], based on the consideration chlorine and sulfur can be fully released during the pyrolysis and char stages of biomass combustion. Mass fractions of KOH, HCl and SO_2 in the volatile can then be obtained, as shown in Table 2. The detailed alkali mechanism developed by Glarborg and Marshall [21] includes elementary reactions over Na, K, C, H, O, S and Cl. Here, the element Na is not considered, which leads to a detailed mechanism of potassium involving 35 species and 153 elementary reactions.

To study the potassium reactions under the premixed condition, a 1D freely propagating premixed flame of the biomass volatile is simulated using CANTERA [42]. The inlet volatile-air mixture temperature is 300 K and three equivalence ratios, i.e., ϕ = 0.5, 1.0 and 2.0, of the mixture are considered. To investigate the diffusion condition, a 1D counterflow diffusion volatile flame is simulated also using CANTERA [42]. The mass flow rates of the biomass volatile and air inlets are 0.024 (kg/m^2 s) and 0.072 (kg/m^2 s), respectively, while their temperatures both are 300 K. Four configurations with HCl and/or SO_2 replaced by N_2 are set up to study the effects of HCl and SO_2 on potassium reaction characteristics. In total 16 cases are simulated. The grid is limited to 250 points while the length of the 1D computational domain for premixed and diffusion condition is 1.0 m and 3.0 cm, respectively.

3. Pulverized-biomass flame configuration and numerics

A two-dimensional temporally evolving pulverized-biomass jet flame is studied (Fig. 1). The computational domain has physical dimensions of 51.2 mm in both the streamwise (x) and spanwise (y) directions. A uniform mesh of h = 100 μm is used, which has been demonstrated to be able to resolve the flame structure [26]. Initially, high-speed primary air (10 m/s, 300 K) laden with pulverized-biomass particles is set up for $|y|$ < 2.5 mm, and the 902 biomass particles follow a random uniform distribution. The initial density of a particle is set to 550 kg/m^3 [43] and its diameter is 25 μm, following a mono-disperse diameter distribution. The particle diameter used here might be finer than common diameters of pulverized-biomass employed in other studies, e.g., 60–200 μm [12, 44]. However, the particle diameter cannot be larger in order to fulfill the grid resolution required by DNS and the point-particle assumption. On the other hand, this fine diameter of 25 μm can be achieved with torrefied biomass [44]. Same as the 1D simulations, properties of corn straw [16] are employed (Table 1). Surrounding the primary air, a hot coflow (3 m/s, 1519 K) is introduced with a composition and temperature of the burnout gas of the biomass volatile at an equivalence ratio of 0.45. Periodic boundary conditions are employed in all directions. Turbulent fluctuations of 0.05 m/s are initially put within the shear layers between the primary air and the coflow, for the purpose of facilitating the jet development. The parameters of the present configuration are chosen according to our previous study on pulverized-coal flames [26, 45]. Two-way coupling between the gas and particle phases are considered and biomass particles are treated as point sources.

Biomass pyrolysis, including K/Cl/S release, volatile-gas combustion and K/Cl/S reactions are simulated. Heterogeneous reaction of solid char is not considered, since its contribution has been demonstrated to be weak in small-scale pulverized-coal flames [32, 34, 46]. The char content of biomass is much lower than that of coal (see Table 1). Hence, the contribution of char combustion in the present pulverized-biomass flame should be even weaker and therefore can be safely ignored.

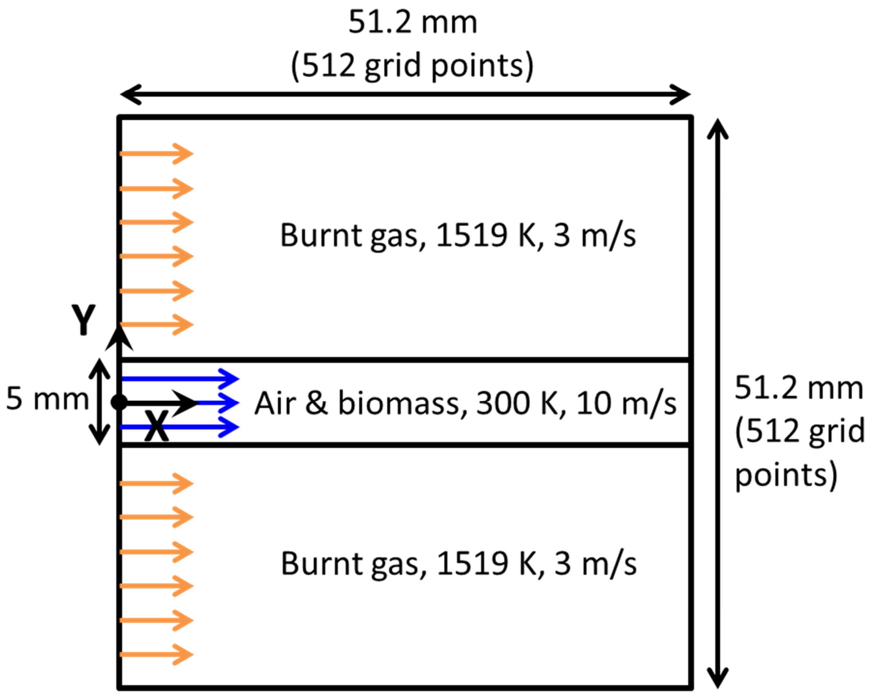

Figure 1. Schematic diagram of computational configuration. Periodic boundary conditions in all directions

3.1. Gas phase modeling

The governing equations for the gas and biomass-particle phases are solved in the Eulerian and Lagrangian frameworks, respectively, using a low-Mach-number in-house code [26, 30, 33, 34]. The conservation equations for mass, momentum, species and temperature solved for the gas phase are:

$$\mathrm{D}_t\rho = \dot{S}_{m,p} \tag{1}$$

$$\mathrm{D}_t\left(\rho u_i\right) = -\partial_i p + \partial_j \tau_{ij} + \dot{S}_{mom,p,i} \tag{2}$$

$$\mathrm{D}_t\left(\rho Y_n\right) = \partial_j\left(\rho D_n \partial_j Y_n\right) + \dot{\omega}_{Y,n} + \dot{S}_{Y,p,n} \tag{3}$$

$$\mathrm{D}_t\left(\rho T\right) = \partial_j\left(\frac{\lambda}{C_{P,g}}\partial_j T\right) + \frac{\lambda}{C_{P,g}^2}\partial_j C_{P,g}\partial_j T + \dot{\omega}_T + \dot{S}_{T,p} + \dot{S}_{T,R} \tag{4}$$

where $\mathrm{D}_t(\Phi) = \partial_t(\Phi) + \partial_j(\Phi u_j)$, $\partial_j \equiv \partial x_j$, ρ is gas density (kg/m^3), u_i is gas velocity (m/s), Y_n is the mass fraction of the nth chemical species, T is gas temperature (K). The pressure is denoted by p, and $\tau_{ij} = \mu(\partial_j u_i + \partial_i u_j - 2/3\ \partial_k u_k \delta_{ij})$ is the viscous stress tensor. D_n is the molecular mass diffusivity coefficient (m^2/s), $C_{P,g}$ and λ are the specific heat capacity (J/kg K) and thermal conductivity (W/m K) of the gas mixture, respectively. $\dot{S}_{m,p}$, $\dot{S}_{mom,p,i}$, $\dot{S}_{Y,p,n}$ and $\dot{S}_{T,p}$ are the two-way coupling terms considering the effects of particles on the gas. $\dot{\omega}_{Y,n}$ is the source term due to homogeneous chemical reactions. In the temperature equation, the radiative heat transfer ($\dot{S}_{T,R}$), heat exchange between the gas phase and biomass particles ($\dot{S}_{T,p}$), and thermal effects of homogeneous reactions ($\dot{\omega}_T$) are taken into consideration. In the present study, the Lewis number (Le = 1.0) and Prandtl number (Pr = 0.7) are assumed to be constant.

3.2. Particle phase modeling

The momentum equation of a Lagrangian biomass particle is:

$$\mathrm{d}_t u_{p,j} = f\left(u_j - u_{p,j}\right)/\tau_p \tag{5}$$

where $u_{p,j}$ is the particle velocity (m/s). The dynamic response time (s) of a particle is $\tau_p = \rho_p d_p^2 / 18\mu$, where ρ_p is the density of the particle (kg/m^3), and d_p is its diameter (m). f is the drag coefficient, which considers both the high particle Reynolds number effects and the blowing effects of volatiles at the particle surface [47].

The particle temperature equation can be written as:

$$\mathrm{d}_t T_p = \left(Q_{conv} + Q_{rad} + Q_{dev}\right) / \left(m_p C_{P,p}\right) \tag{6}$$

where T_p is the temperature of the particle (K), m_p its mass (kg), $C_{P,p}$ its specific heat capacity (J/kg K). The heat transfer terms by convection, radiation, and pyrolysis (devolatilization) are $Q_{conv} = \mathrm{Nu} C_{P,g} m_p \left(T - T_p\right) / 3 \,\mathrm{Pr}\, \tau_p$, $Q_{rad} = \varepsilon_p \pi d_p^2 \sigma \left(T_R^4 - T_p^4\right)$, and $Q_{dev} = -\Delta h_{dev}\, \mathrm{d}m_{vol} / \mathrm{d}t$, respectively. Nu is the Nusselt number and computed by the Ranz-Marshall correlations [48]. The radiation temperature (K) is calculated by $T_R = (G/4\sigma)^{1/4}$, where G is the incident radiation (W/m^2) obtained via the Discrete Ordinates Method (DOM) [49]. σ is the Stefan-Boltzmann constant (5.67×10^{-8} W/m^2 K^4). ε_p is the particle emissivity and here is set to 0.9 [39]. The weighted-sum-of-the-gray-gases model (WSGGM) [50] is employed to estimate the gas absorption coefficient. Finally, the mass loss rate of each biomass particle ($\mathrm{d}m_p/\mathrm{d}t$), due to the pyrolysis, is predicted by the single first-order reaction model (SFOM) proposed by Badzioch and Hawskley [51]. The kinetic parameters of the SFOM pyrolysis model, i.e., A_v (2.5×10^9 s^{-1}), E_v (11×10^4 J/mol) and Q_v (1.10), have been calibrated by the bio-CPD model [38], as in [30, 33, 34].

3.3. Gas phase chemistry

Same as in Section 2, the oxidization of hydrocarbon biomass volatile and the reactions of potassium species are modeled by the DRM22 skeletal mechanism [37] and the detailed alkali reaction mechanism [21], respectively. The compositions of the volatile gas can be found in Table 2, including the non-hydrocarbon compounds of potassium, sulfur and chloride.

The release rate of potassium from biomass particles is assumed to be proportional to the volatile release rate [26, 34], since the potassium vapor generated inside the porous structure of a biomass particle will be transported outward by the volatile yielded during the pyrolysis stage. Besides, in our previous study the alkali release from a coal particle was found proportional to its burnout during the early combustion stage [18]. Similarly, the release rates of sulfur and chlorine are also assumed to be proportional to the volatile release rate here.

3.4. Numerical schemes

The numeric of our in-house code is based on an approach previously validated for both DNS and LES [52, 53]. A second-order Crank-Nicolson scheme is employed for the time advancement. A second-order central difference scheme is applied to all terms in the momentum equation and the scalar diffusion terms in the species and temperature equations. In order to secure the scalar boundedness, a Quadratic Upstream Interpolation for Convective Kinematics (QUICK) scheme is used for the scalar advection terms in the species and temperature equations. An Alternating Direction Implicit (ADI) approach has been adopted, and semi-implicit tridiagonal/pentadiagonal equations are solved separately for each direction. A second-order Runge-Kutta (RK2) scheme is employed to explicitly advance the particle equations.

4. Results and discussion

4.1. Transformation characteristics of potassium species in 1D premixed flame

The reactions of potassium species in 1D premixed volatile flames have been investigated for three equivalence ratios (ϕ = 0.5, 1.0 and 2.0), representing fuel-lean, stoichiometric and fuel-rich conditions. From Fig. 2, it can be found that the concentration of KOH rapidly decreases in the initial unburned region with $T = 300$ K, which should be attributed to the following two reaction paths:

$$2KOH \rightarrow K_2O_2H_2 \ (R1);$$

$$KOH + HCl \rightarrow KCl + H_2O \ (R2), \quad 2KCl \rightarrow K_2Cl_2 \ (R3).$$

First, KOH is consumed to generate $K_2O_2H_2$ via Reaction R1. In addition, KOH also reacts with HCl in the volatile as Reaction R2, and K_2Cl_2 is subsequently formed through Reaction R3. $K_2O_2H_2$ and K_2Cl_2 are the two major potassium species in the initial unburned region. It should be noted that at low temperature, the potassium is in condensed form, possibly as aerosol. Hence, the results in the initial unburned region of the canonical laminar flame are questionable. However, this issue will get relieved in the following investigation of 2D pulverized-biomass flame (Section 4.3) because the potassium is released along with volatile and therefore at much higher temperature. When the combustion happens and therefore the temperature increases around Distance of 0.15 cm, $K_2O_2H_2$ and K_2Cl_2 are then decomposed to KOH and KCl, respectively, and further transform to other potassium species, e.g., K, KO_2, KSO_2, $KHSO_4$ and K_2SO_4. In the post-flame region, the potassium species then gradually evolve towards equilibrium. It can be observed that KOH is the most significant potassium product (~10^3 ppm) for all the three equivalence ratios, while KCl has the second highest concentration (~10^2 ppm). The sulfurous potassium species K_2SO_4 is found to be the third major potassium product (34 ppm) under the fuel-lean condition; while under the stoichiometric and fuel-rich conditions, the third major potassium product changes to atomic potassium K (> 60 ppm). Another minor potassium species, KSO_3Cl, has a maximum concentration less than 0.01 ppm during the whole reaction process for all the three equivalence ratios and therefore is not shown in the figure.

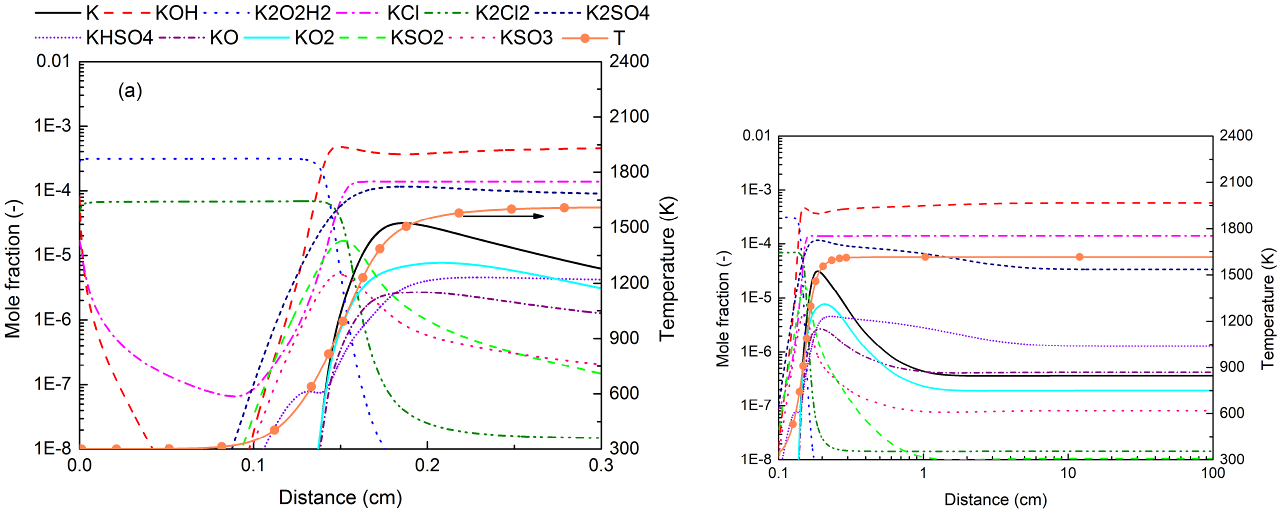

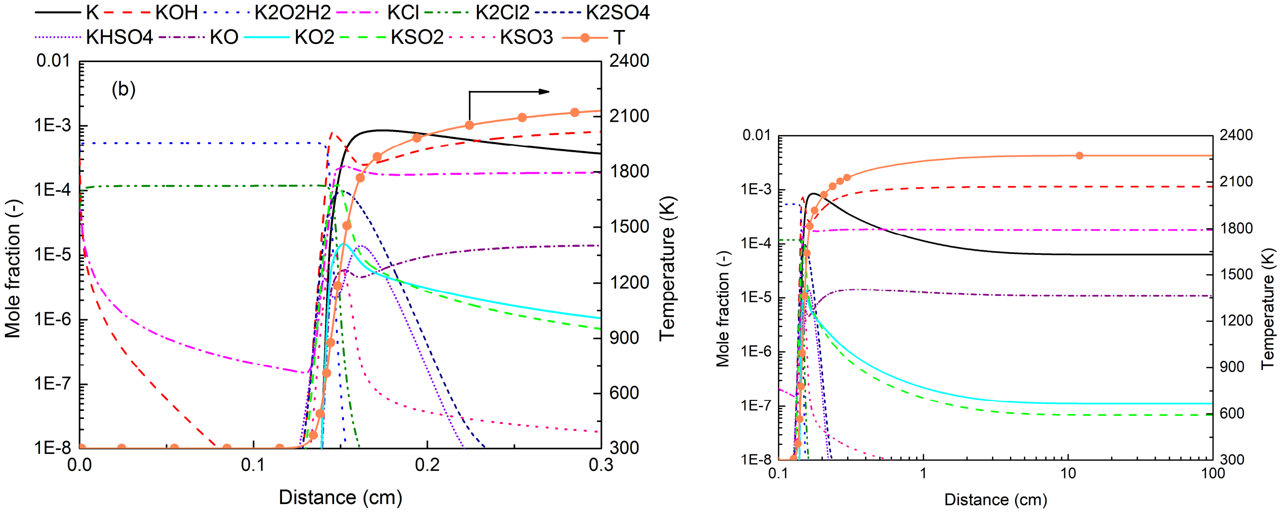

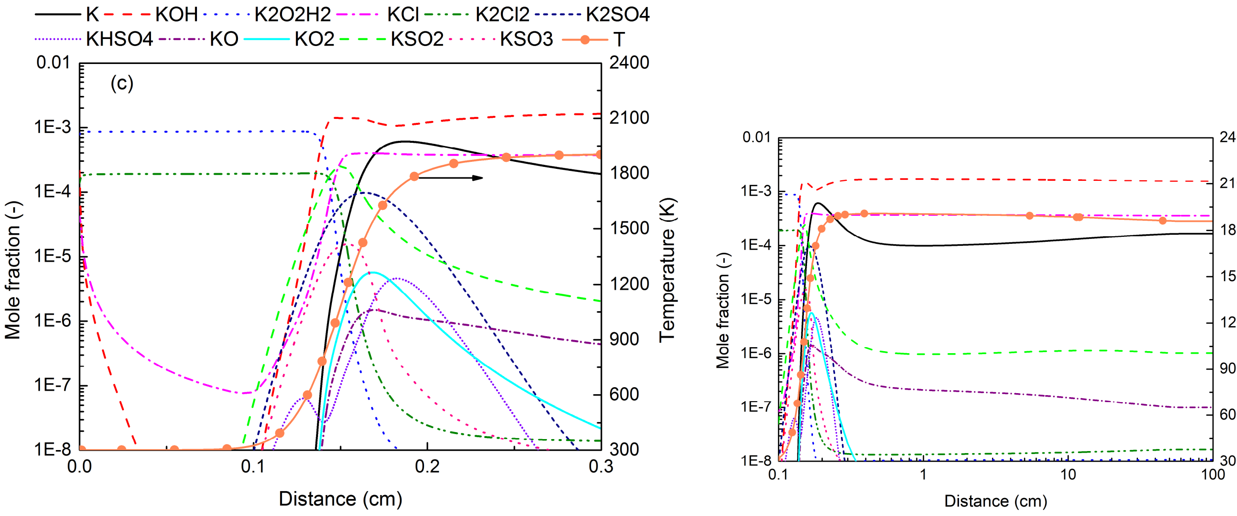

Figure 2. Potassium species distribution versus distance along the 1D premixed volatile flame at equivalence ratio ϕ = 0.5 (a), ϕ = 1.0 (b) and ϕ = 2.0 (c). The heat release zone is zoomed in and shown on the left side while the overall flame is shown on the right side.

To study the effects of HCl and SO_2 on potassium transformation characteristics, three additional configurations have been employed, which are Case B (HCl in the volatile is replaced by N_2), Case C (SO_2 in the volatile is replaced by N_2) and Case D (both HCl and SO_2 in the volatile are replaced by N_2). The original case is referred to as baseline Case A. Three simulations (ϕ = 0.5, 1.0 and 2.0) are performed for each Case A/B/C/D. The comparison of the representative potassium species KOH, KCl and K_2SO_4 is shown in Fig. 3. The profiles are plotted until Distance of 10 cm, as it can be found in Fig. 2 that the potassium reactions almost reach equilibrium at this position. KOH is found to be the main potassium product for the four cases. When HCl and/or SO_2 is presented, a minor part of potassium is transformed to KCl and/or K_2SO_4. However, the mole fraction of the produced KCl and/or K_2SO_4 is much lower than that of KOH. Hence, the profiles of KOH are close to each other for the four cases in the combustion and post-flame regions.

274

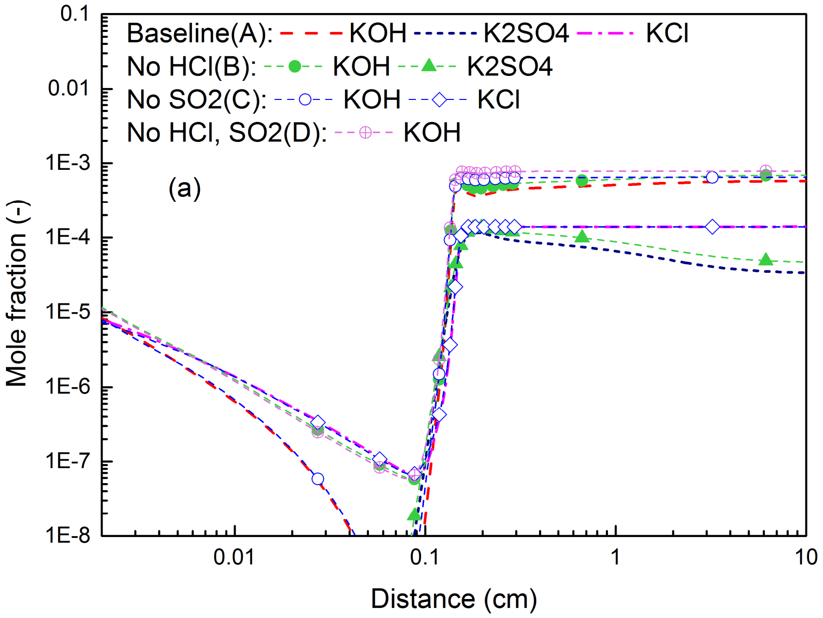

275

276

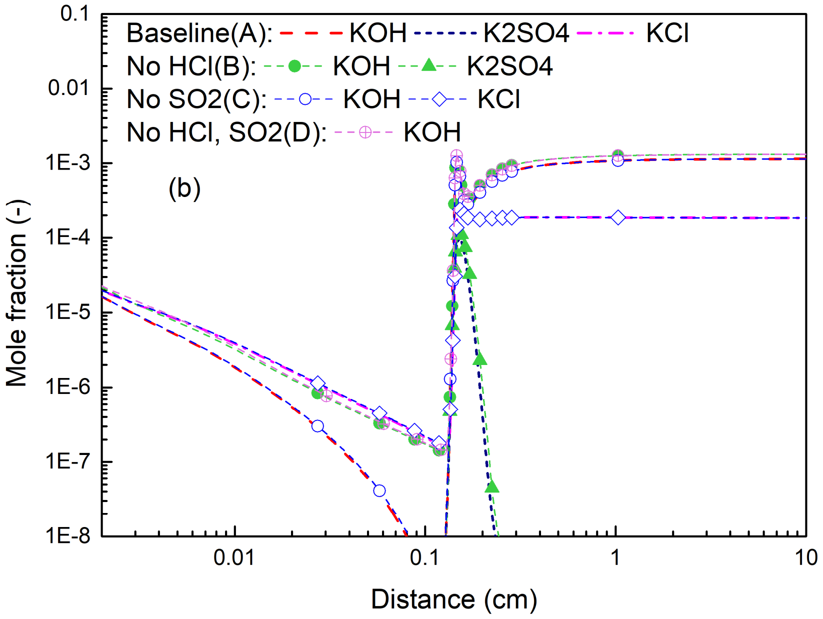

277

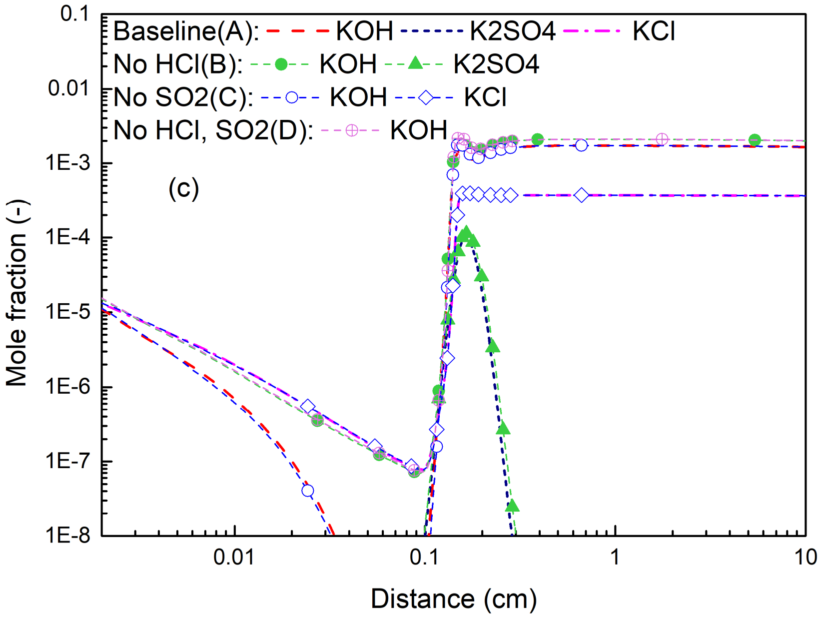

Figure 3. Comparison of potassium species distribution versus distance along the 1D premixed volatile flame between Case A (the baseline case), Case B (HCl replaced by N_2), Case C (SO_2 replaced by N_2) and Case D (both HCl and SO_2 replaced by N_2) at equivalence ratio $\phi = 0.5$ (a), $\phi = 1.0$ (b) and $\phi = 2.0$ (c).

4.2. Transformation characteristics of potassium species in 1D diffusion flame

To further investigate the response of potassium species in diffusion flame, other four cases have been set up: Case E (the baseline case), Case F (HCl in the volatile is replaced by N_2), Case G (SO_2 in the volatile is replaced by N_2) and Case H (both HCl and SO_2 in the volatile are replaced by N_2). Comparison among these cases on the representative potassium species K, KOH, KCl and K_2SO_4 is shown in Fig. 4. It may be noted that only the region of the mixture fraction $Z < 0.6$ are shown, because a higher mixture fraction is hardly observed in the following 2D DNS study (see Fig. 7 below). The mixture fraction could be calculated as $Z = 1.0 - Y_{N2}/0.767$. For the present two-stream mixing case of 1D diffusion flame, $Z = 0$ and $Z = 1$ indicate the oxidizer and biomass-volatile streams, respectively. The positions of $\phi = 0.5$, 1.0 and 2.0 in the mixture fraction space are also illustrated in Fig. 4. It can be found that in the fuel-lean region the mole fraction of K increases rapidly with Z for all the cases. In the very rich region of $Z > 0.5$, the profile of K drops in the cases (E/F) with SO_2, which is not observed in the cases (G/H) without SO_2. Both KOH and KCl show a monotonically increasing trend along with *Z*, although the increasing rate get suppressed at the stoichiometric condition. For Na_2SO_4, it reaches a concentration of ~20 ppm at the fuel-lean region around *Z* = 0.05, but becomes minor (< 0.1 ppm) for all the other conditions. Similar as in the previous premixed flames, the profiles of KOH in the four cases here are also close to each other, because the productions of sulfurous and chloric potassium species are limited.

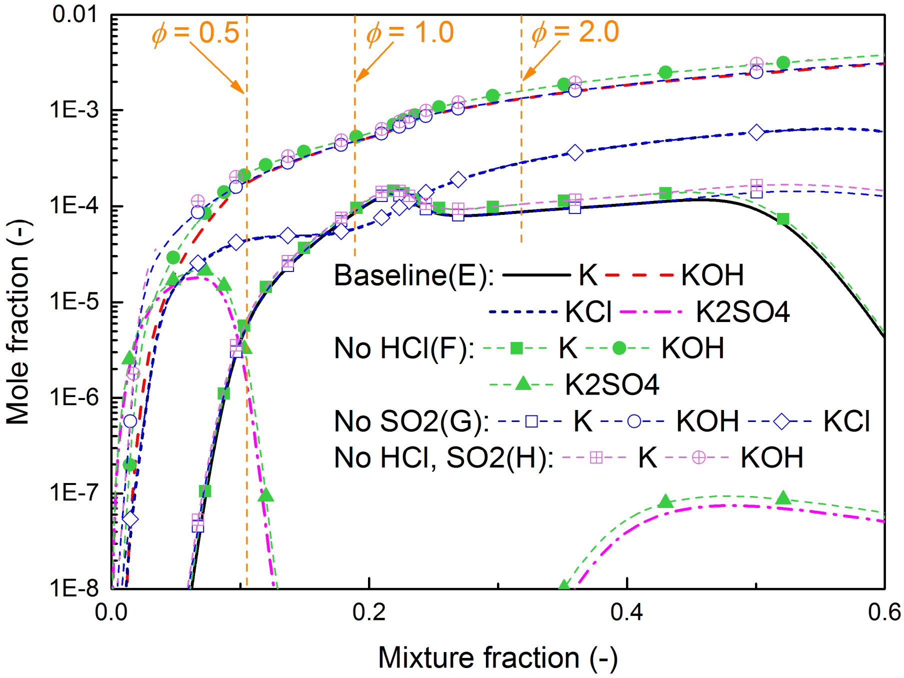

Figure 4. Comparison of potassium species distribution in the mixture fraction space of the 1D diffusion volatile flame among Case E (the baseline case), Case F (HCl replaced by N_2), Case G (SO_2 replaced by N_2) and Case H (both HCl and SO_2 replaced by N_2).

4.3. Characteristics of the 2D pulverized-biomass flame

The transformation of potassium species in the 2D pulverized-biomass flame is then sequentially examined. Figure 5 shows the evolution of some important quantities of the flame: (a) gas temperature and particle burnout, (b) OH mass fraction, (c) K mass fraction, (d) KOH mass fraction, and (e) flame index and particle temperature. In the early stage of *t* = 10–15 s, biomass particles in the jet shear layers are heated by the high-temperature coflow. Volatiles including potassium, chlorine and sulfur compounds are then released from these particles via the pyrolysis process. Isolated flame structures [27, 34] can be observed at t = 15 ms, which are formed due to individual particles ignited in the shear layers. At t = 20 ms, more and more particles get ignited and Y_{OH} propagates, representing a strong heat release of the rapid spreading flame. Atomic potassium K has a high concentration in the high-temperature burning zone, while KOH accumulates around the ignited particles. Finally, at t = 30 ms, the flame tends to be weak as most of the biomass particles in the computational domain burn out. However, a wider flame regime can be observed since the turbulent mixing continues. The concentrations of OH radical and atomic K drop, but that of KOH remains a significant level.

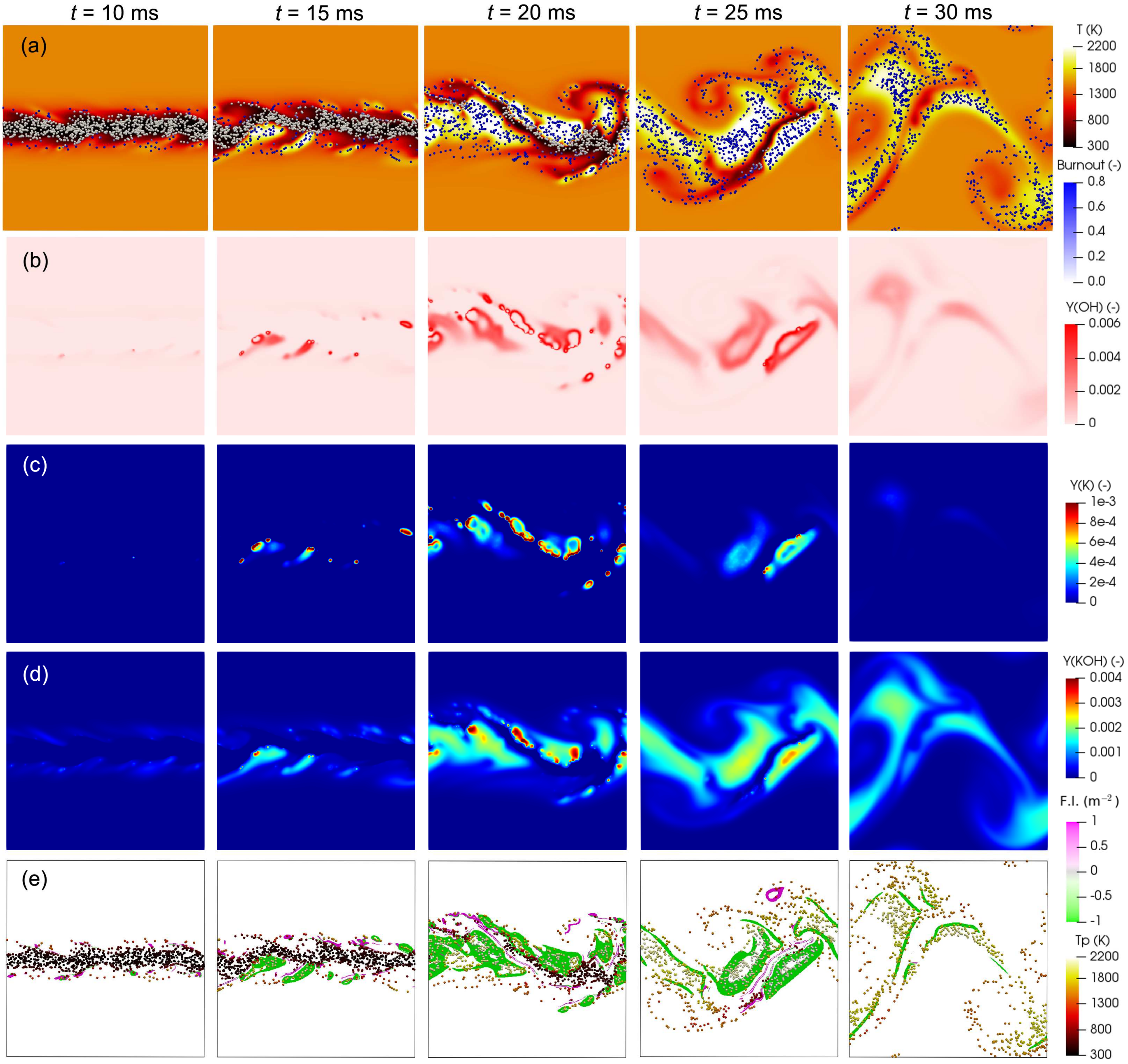

Figure 5. Time evolutions of instantaneous distributions of the (a) gas temperature and particle burnout, (b) OH mass fraction, (c) K mass fraction, (d) KOH mass fraction and (e) flame index and particle temperature.

Based on the spatial gradients of the mass fractions of volatile fuel and oxidizer, the flame index, F.I. [24, 54, 55], can be computed as: F.I. = $\nabla Y_f \cdot \nabla Y_{O2}$, where $Y_f = Y_{CH4} + Y_{CO} + Y_{C2H2} + Y_{H2}$. Positive F.I. values indicate premixed flame regimes, while negative ones for diffusion flame. F.I. distribution of the biomass flame is shown in Fig. 5e for the regions where the heat release rate exceeds 10^7 W/m^3 and therefore are actively reacting regions. The maximum heat release rate in the 2D domain is 3.03×10^{10} W/m^3. It can be found that at the beginning stage of $t < 15$ ms, the first ignition of biomass particles is controlled by premixed combustion. Then after the biomass jet reaches actively reacting state, the volatile released from particles accumulates before burning and therefore leads to a dominant diffusion combustion mode [26].

Figure 6 shows the instantaneous distributions of all the twelve potassium species considered in the DNS at $t = 20$ ms. The isoline of $\phi = 1$ is superimposed, which represents the stoichiometric condition of combustion between the biomass volatile and the oxidizer. It can be found that atomic K has a high concentration in the regime close to the isoline, where the volatile fuel is actively burning and the temperature is high. Both KOH and KCl feature a high concentration in the fuel-rich region (inside the isoline), and a moderate concentration in the fuel-lean region (outside the isoline). KOH is the released potassium species along with the volatile, while the high concentration of KCl in the fuel-rich region can be explained by the Reaction R2. $KHSO_4$ and K_2SO_4 are the two major sulfated potassium species, which mainly form in the fuel-lean region, but their concentrations are much lower than the potassium chloride KCl. The two favored potassium species in the pre-combustion mixture K_2Cl_2 and $K_2O_2H_2$ are observed only in the fuel-lean region, since they will decompose under high temperature. The other five minor potassium species, i.e., KO, KO_2, KSO_2, KSO_3 and KSO_3Cl, are produced under the fuel-lean condition, while KSO_2 achieves a high concentration in the fuel-rich region where abundant potassium and sulfur exist.

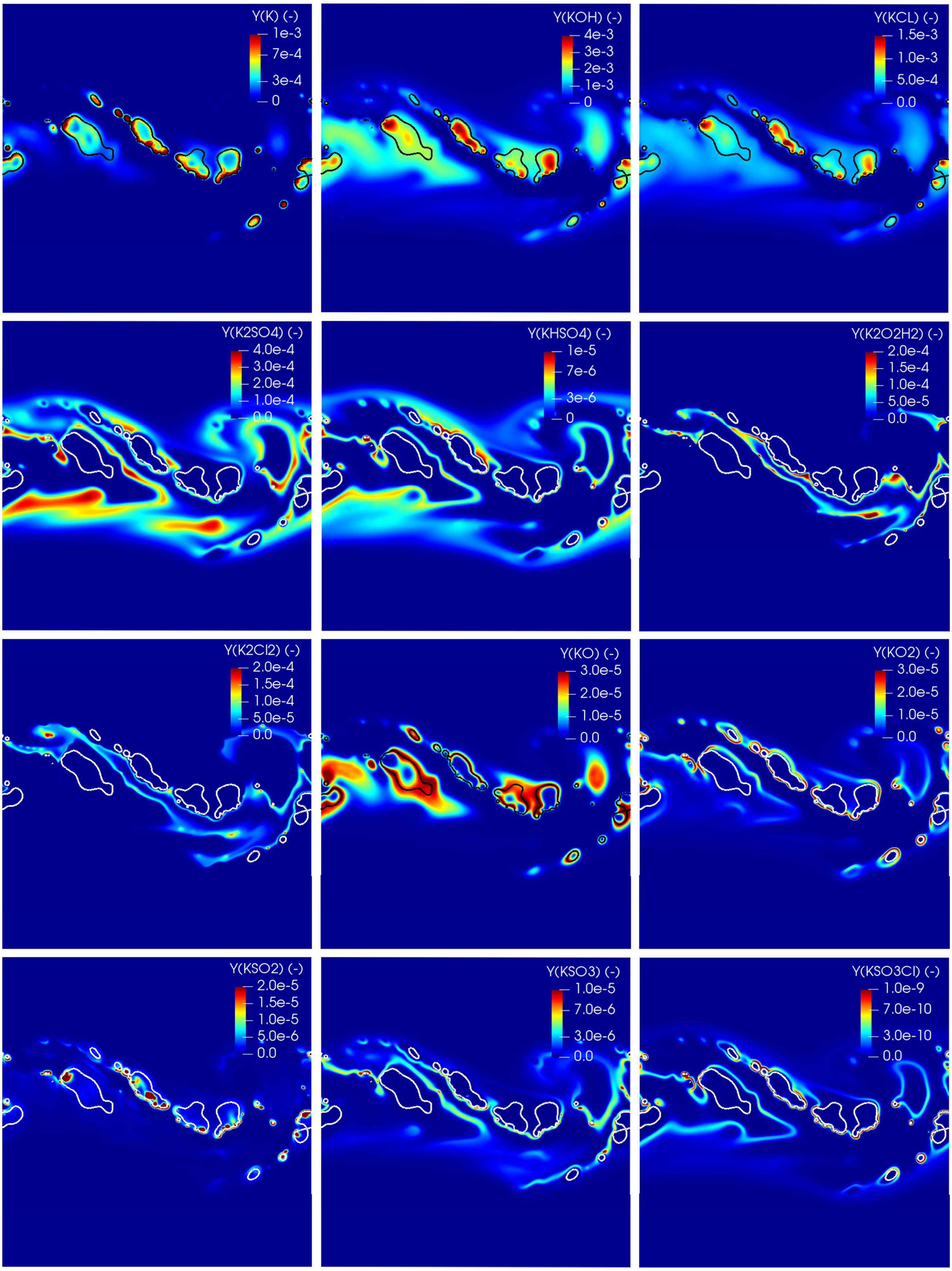

Figure 6. Instantaneous distributions of all the twelve potassium species at t = 20 ms. The isoline of ϕ = 1 is superimposed.

4.4. Potassium species dynamics

Figure 7 shows the instantaneous scatter plots of six representative potassium species against the mixture fraction at t = 20 ms. For the three-stream mixing in the 2D pulverized-biomass flame, the mixture fractions of the volatile released from biomass particles (the fuel stream), the air jet carrying these particles (the oxidizer stream) and the high-temperature coflow are $Z = 1$, $Z = 0$ and $Z = 0.093$, respectively. K, KCl and KOH are the three major potassium species in the reaction products. The distributions of Y_{KCl} and Y_{KOH} are almost linear with Z, while that of Y_{K} is subtler. Y_{K} stays almost zero for the lower range of $Z < 0.05$, to then increases rapidly until $Z = 0.22$, and then holds a moderate increasing rate for the fuel-rich regime of $Z > 0.22$. Finally, Y_{KHSO4}, Y_{K2SO4} and Y_{K2O2H2} feature a single-peak distribution within the fuel-lean regime of $Z < Z_{\mathrm{st}} = 0.189$.

The potassium profiles obtained from 1D diffusion flames are also shown in Fig. 7 with the blue solid line and the red dash line corresponding to the lowest and highest strain rates, respectively. It can be found that the high-strain rate (red dash line) helps to enhance the transformation of KOH to K, $KHSO_4$ and K_2SO_4, while the production of KCl is insensitive to the strain rate. This is because the KCl-formation reactions are almost instantaneous (of the order of a few micro seconds), and therefore can hardly be affected by the relatively much slowly varying strain rate. It can also be observed in Fig. 2 that the reaction zone of KCl is much thinner than the other potassium products. Compared with the line plots from 1D diffusion flames, the DNS scatters generally follow a similar trend, but lots of data points fall outside the region between the red dash and blue solid lines. These points are likely to represent the unsteadiness and/or partial premixing of the reactants, because the volatile ejected from the particles is rapidly mixed with the ambient air in a partially premixed mode, as in [56]. Besides, the radiation heat loss also contributes to the discrepancy between line plots from

1D diffusion flames and DNS scatters.

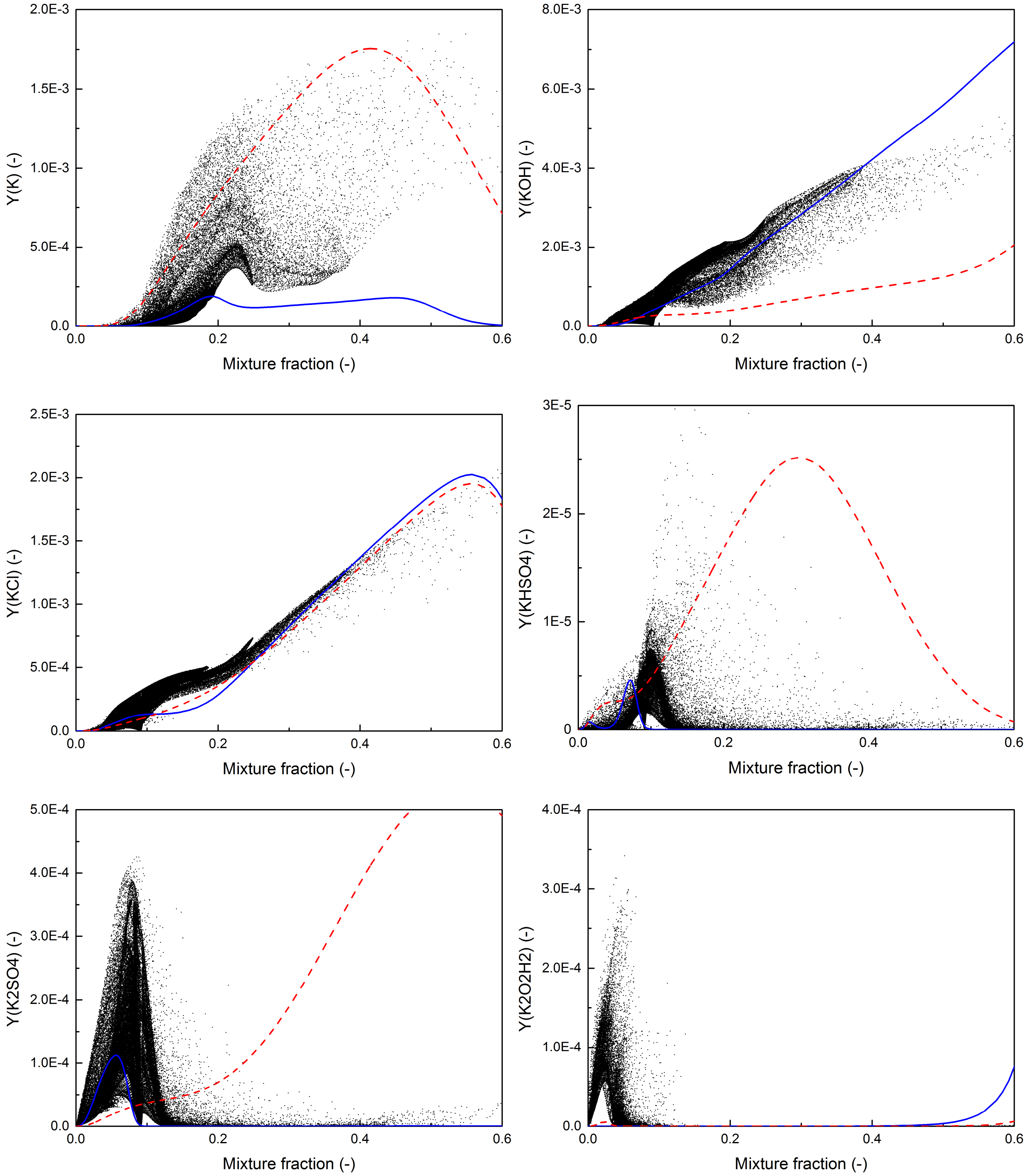

Figure 7. Scatter plots of instantaneous mass fractions of K, KCl, KOH, $KHSO_4$, K_2SO_4 and $K_2O_2H_2$ against Z at t = 20 ms. Blue solid line and red dash line are the potassium profiles obtained from 1D counterflow diffusion flames, corresponding to the lowest (21 s^{-1}) and highest strain rates (8556 s^{-1}).

4.5. Statistics of the 2D pulverized-biomass flame

Figures 8 and 9 show the time evolutions of the mean mass fractions of OH, HCl, SO_2, Z_{vol} and six representative potassium species, and the mean gas temperature of the biomass flame. All of these quantities are averaged over the entire 2D computational domain. Z_{vol} is the volatile mixture fraction, which can be obtained from:

$$\mathrm{D}_t\left(\rho Z_{vol}\right)=\partial_j\left(\rho D_Z \partial_j Z_{vol}\right)+\dot{S}_{Y,p,vol} \tag{7}$$

where D_Z is the diffusivity coefficient of volatile gas (m^2/s) and its value is set equal to the thermal diffusivity. $\dot{S}_{Y,p,vol}$ is the source term of the volatile mass released from biomass particles.

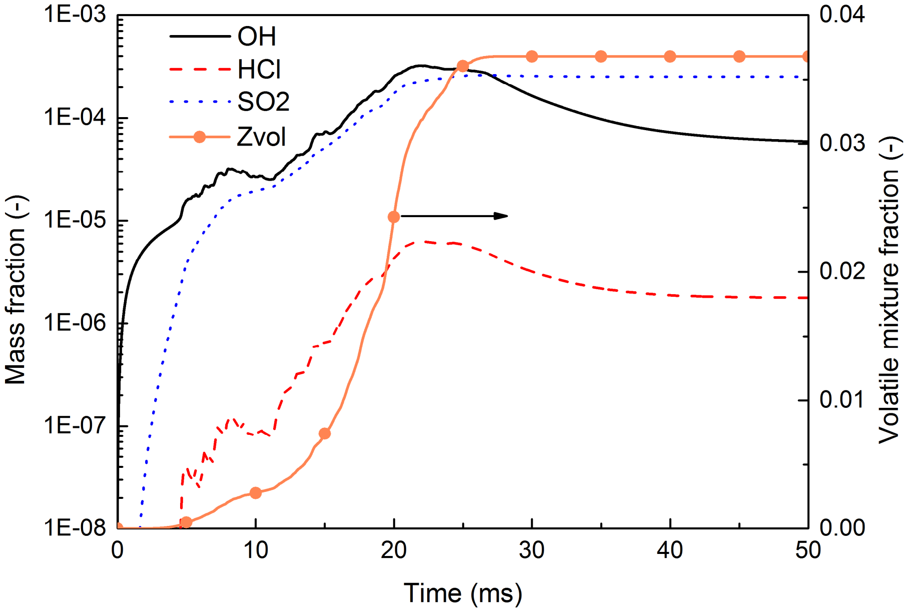

Figure 8. Time evolutions of the mean mass fractions of OH, HCl, SO_2 and Z_{vol} averaged over the 2D computational domain.

It can be observed that the first ignition of the biomass jet happens at t = 5 ms. The mass fractions of potassium species and the gas temperature start to increase and small peaks can be found for Y_{OH} and Y_{HCl}. This is because the volatile fuel gets ignited around some particles, which in turn heats up the particles rapidly and therefore bring a high flux of volatile release. After t = 15 ms, the biomass jet is actively burning which reflects in both T and Z_{vol} increase rapidly, same as the mass fractions of Y_{OH}, Y_{HCl}, Y_{SO2}, Y_{KOH} and Y_{KCl}. After t = 30 ms, both T and Z_{vol} remain almost constant, indicating the end of the combustion of the biomass jet. However, although the average of gas temperature in the domain becomes stable, its variance is further decreasing due to turbulent mixing of the hot burnout gases and the surroundings. This explains the variation of the species mass fractions after t = 30 ms, e.g. the decreasing of Y_{HCl} due to Reaction R2. At the end of the simulation (t = 50 ms), KOH is found to be the major potassium product. Comparing the DNS predictions at the end of the simulation to a reference equilibrium calculation by CANTERA [42] of a zero-dimensional (0D) homogeneous reactor under the temperature of 1538 K, which is the final averaged temperature of the 2D DNS domain, the relative departures are of 2.07% for KOH, 2.93% for KCl and 21.85% for K_2SO_4. The results indicate KOH and KCl are largely equilibrated while K_2SO_4 is kinetically limited. The larger departure for K_2SO_4 should be attributed to the slower sulfation reactions, as shown in Fig. 2a, and therefore it would take a much longer time for K_2SO_4 to reach equilibrium. Furthermore the 2D DNS domain does not reach a homogeneous state at t = 50 ms, which also contributes to the difference between the DNS predictions and equilibrium results.

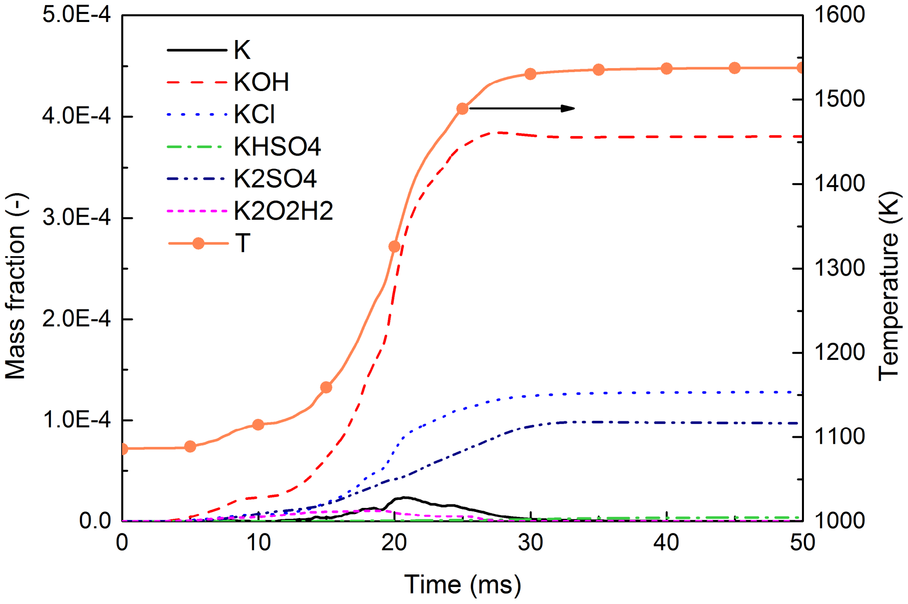

Figure 9. Time evolutions of the mean mass fractions of K, KOH, KCl, $KHSO_4$, K_2SO_4 and K_2Cl_2, and the mean gas temperature.

The major pathways of potassium transformation in the pulverized-biomass flame is summarized in Fig. 10. It can be found that HCl reacts with potassium species in a straightforward way, i.e., $HCl + KOH \rightarrow KCl + H_2O$ and $HCl + K \rightarrow KCl + H$. In contrast, the formation of sulfated potassium species is more complex. The SO_2 is first oxidized to SO_3, to then reacts with KOH to form $KHSO_4$, and finally produce K_2SO_4 through a shuffle reaction, $KHSO_4 + KOH \rightarrow K_2SO_4 + H_2O$.

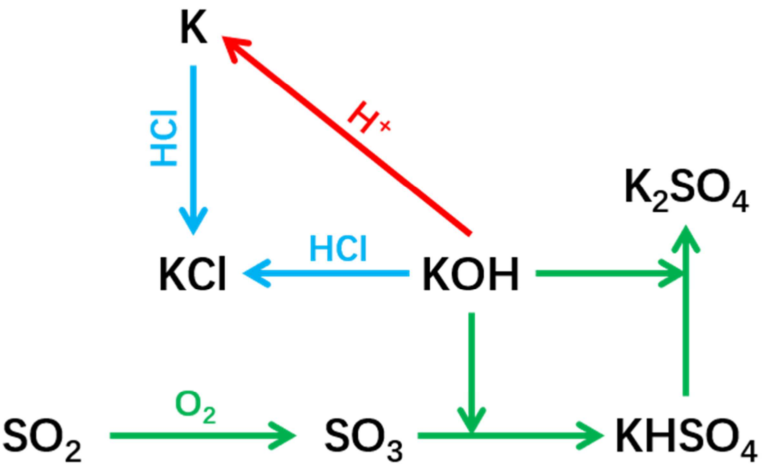

Figure 10. Major pathways of potassium transformation during pulverized-biomass combustion.

4.6. Effects of HCl and SO_2 on potassium emissions in the 2D pulverized-biomass flame

Three additional DNS cases are set up to investigate the effects of HCl and SO_2 on potassium transformation characteristics: Case K (HCl in the volatile is replaced by N_2), Case L (SO_2 in the volatile is replaced by N_2) and Case M (both HCl and SO_2 in the volatile are replaced by N_2). Case J refers to the original baseline DNS case. The comparison between the four cases is shown in Figure 11. In all the cases, KOH is the main potassium product at the end of the simulation. However, with HCl and/or SO_2 present, part of KOH is transformed to KCl and/or K_2SO_4, respectively. Based on the initial mass fractions (Y_0) of KOH/HCl/SO_2 in the volatile (Table 2) and the final mass fractions (Y_{final}) of KCl/K_2SO_4 in the burnout gases, we can calculate the conversion rate (α) of KCl and

K_2SO_4 as:

$$\alpha_{\mathrm{KCl}} = \frac{Y_{\mathrm{final,KCl}}/M_{\mathrm{KCl}}}{Z_{vol,\mathrm{final}} \cdot \min\left(Y_{0,\mathrm{KOH}}/M_{\mathrm{KOH}}, Y_{0,\mathrm{HCl}}/M_{\mathrm{HCl}}\right)} \times 100\% \tag{8}$$

$$\alpha_{\mathrm{K_2SO_4}} = \frac{Y_{\mathrm{final,K_2SO_4}}/M_{\mathrm{K_2SO_4}}}{Z_{vol,\mathrm{final}} \cdot \min\left(0.5Y_{0,\mathrm{KOH}}/M_{\mathrm{KOH}}, Y_{0,\mathrm{SO_2}}/\mathrm{M}_{\mathrm{SO_2}}\right)} \times 100\% \tag{9}$$

where M denotes the molar mass. The obtained conversion rate of KCl in Case L is $\alpha_{\mathrm{KCL}} = 95.1\%$, while that of K_2SO_4 in Case K is $\alpha_{\mathrm{K2SO4}} = 14.7\%$. The conversion rate of KCl is much higher than that of K_2SO_4, indicating HCl has a much stronger ability to react with potassium species than SO_2.

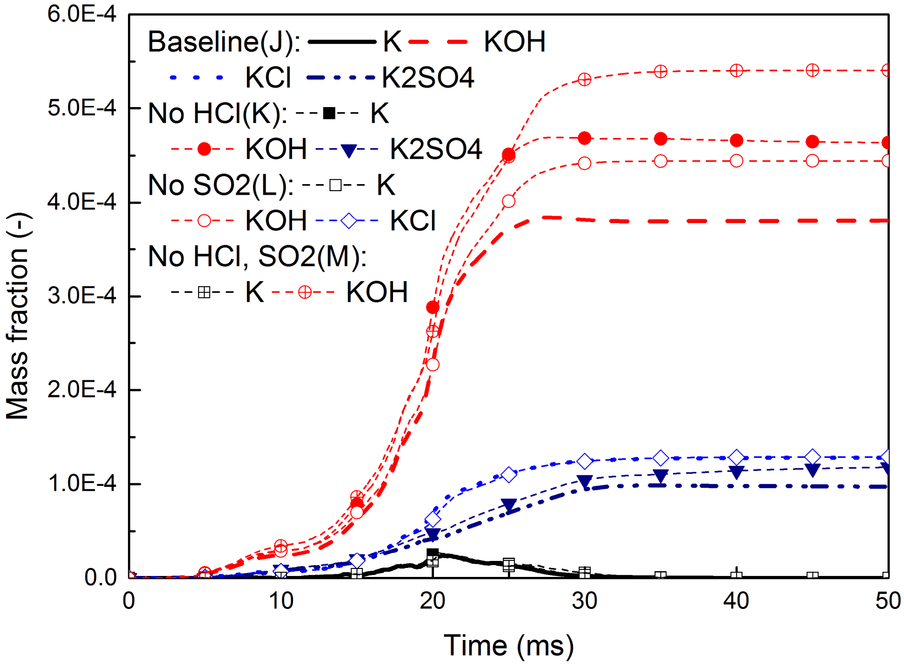

Figure 11. Comparison of time evolutions of the mean mass fractions of potassium species among Case J (the baseline case), Case K (HCl replaced by N_2), Case L (SO_2 replaced by N_2) and Case M (both HCl and SO_2 replaced by N_2).

4.7. Comparison of potassium emission characteristics in 1D and 2D flames

The 1D premixed flame simulations (Fig. 2) show that KOH is the most significant potassium product under various equivalence ratios in fuel-lean, stoichiometric and fuel-rich conditions. This is consistent with the 1D diffusion flame simulation results (Fig. 4). However, some discrepancies can be observed between the premixed and diffusion flame predictions. For instance, the premixed flame results show that the second major potassium product is KCl under all the conditions, which is not the case in the diffusion flame under stoichiometric condition, where atomic K has a higher concentration than KCl. The reason of the discrepancy should be that the 1D diffusion flame is strained while the 1D premixed flame is freely propagating. In fact, Fig. 7 indeed shows that a higher strain rate could promote the production of K, while KCl is insensitive to the variation of strain rate. Finally, the statistics of the 2D biomass flame also demonstrates that KOH is the major potassium product. The overall equivalence ratio of the 2D flame is 0.55 (corresponding to a mixture fraction $Z = 0.094$), and therefore its potassium emission statistics are close to that of the 1D flames under the fuel-lean condition.

5. Conclusions

The emission characteristics of potassium species in biomass combustion are numerically investigated via 1D premixed/diffusion flames of biomass volatile, and a 2D pulverized-biomass flame. Complex chemistry has been used for both the volatile hydrocarbon combustion and the potassium species reactions. From the 1D premixed flame simulations, it is found that KOH is the most significant potassium product for all the three equivalence ratios, while KCl has the second highest concentration. The 1D diffusion flame simulations also support that KOH is the major potassium products while the productions of sulfurous and chloric potassium species are secondary.

The emission characteristics of the potassium species in a 2D pulverized-biomass flame are then examined. The instantaneous distribution characteristics show that KOH, KCl and K are the three major potassium species in the reaction zone. The distributions of Y_{KCl} and Y_{KOH} are almost linear with Z, while that of Y_K is more complex. Y_K stays almost zero for the lower range of $Z < 0.05$, to then increases rapidly until $Z = 0.22$, and then holds a moderate increasing rate for the fuel-rich regime of $Z > 0.22$. Y_{KHSO4}, and Y_{K2SO4} are the two main sulfated potassium species which feature a single-peak distribution within the fuel-lean regime of $Z < Z_{st} = 0.189$. The statistics of the 2D simulation also illustrate that KOH is the major potassium product, in consistent with the 1D predictions. Finally, the 2D parametric study reveals that the conversion rate of KCl is much higher than that of K_2SO_4, indicating HCl has a much stronger ability to react with potassium species than SO_2. These fundamental transformation characteristics of potassium revealed in the present study could potentially benefit the development of potassium control technologies and mitigate the fouling and corrosion issues in biomass furnace. For instance, since the conversion rate of K_2SO_4 is found to be relatively low, a relatively high concentration of SO_2/SO_3 might be required to convert the potassium chlorides to sulfates, whose melting temperatures are higher and which are therefore less problematic [57].

It should be noted that the conclusion draw here is based on the biomass of corn straw we used. In the future, this work will be extended with various types of biomass to study the effects of K/Cl and K/S ratios on potassium emission characteristics. Besides, the present numerical study only considers the 1D and 2D simulations, a full three-dimensional (3D) simulation is still required to better investigate the potassium transformation in turbulent flows. Finally, these numerical simulations can be further improved once the suitable release models of potassium, sulfur and chloride for a pulverized-biomass particle become available in the future.

Acknowledgements

This work was jointly supported by the National Natural Science Foundation of China (51706200), the China Postdoctoral Science Foundation (2018M632460), the Fundamental Research Funds for the Central Universities (2018FZA4012), the Engineering and Physical Sciences Research Council (EPSRC) and the Royal Society of the UK. The first author K.D.W. would like to acknowledge the support from the Centre national de la recherche scientifique (CNRS) of the France. Y.L. is funded by the Open Topic Exploration Program of the ZJU CEU laboratory. Special thanks are due to Prof. Peter Glarborg of DTU, who provided us the detailed mechanism of alkali metal species. Computing resources were provided by the National Supercomputer Center in Tianjin, China (http://www.nscc-tj.cn).

References

[1] Hosseini SE, Wahid MA. Utilization of palm solid residue as a source of renewable and sustainable energy in Malaysia. Renewable and Sustainable Energy Reviews 2014;40:621-32.

[2] Niu Y, Tan H, Hui Se. Ash-related issues during biomass combustion: Alkali-induced slagging, silicate melt-induced slagging (ash fusion), agglomeration, corrosion, ash utilization, and related countermeasures. Prog. Energy Combust. Sci. 2016;52:1-61.

[3] Liu Y, Cheng L, Zhao Y, Ji J, Wang Q, Luo Z, et al. Transformation behavior of alkali metals in high-alkali coals. Fuel Process. Technol. 2018;169:288-94.

[4] Capablo J. Formation of alkali salt deposits in biomass combustion. Fuel Process. Technol. 2016;153:58-73.

[5] Liu YZ, He Y, Wang ZH, Xia J, Wan KD, Whiddon R, et al. Characteristics of alkali species release from a burning coal/biomass blend. Appl. Energy 2018;215:523-31.

[6] Fagerström J, Steinvall E, Boström D, Boman C. Alkali transformation during single pellet combustion of soft wood and wheat straw. Fuel Process. Technol. 2016;143:204-12.

[7] Paneru M, Babat S, Maier J, Scheffknecht G. Role of potassium in deposit formation during wood pellets combustion. Fuel Process. Technol. 2016;141:266-75.

[8] Capablo J, Ballester J. Experimental study of the kinetics of sulfation of alkali chloride deposits.

Fuel Process. Technol. 2015;140:215-21.

[9] Ma T, Fan C, Hao L, Li S, Jensen PA, Song W, et al. Biomass ash induced agglomeration in fluidized bed. Part 2: Effect of potassium salts in different gas composition. Fuel Process. Technol. 2018;180:130-9.

[10] Mason PE, Jones JM, Darvell LI, Williams A. Gas phase potassium release from a single particle of biomass during high temperature combustion. Proc. Combust. Inst. 2017;36(2):2207-15.

[11] Mason PE, Darvell LI, Jones JM, Williams A. Observations on the release of gas-phase potassium during the combustion of single particles of biomass. Fuel 2016;182:110-7.

[12] Weng W, Costa M, Aldén M, Li Z. Single particle ignition and combustion of pulverized pine wood, wheat straw, rice husk and grape pomace. Proc. Combust. Inst. 2019;37(3):2663-71.

[13] Weng W, Gao Q, Wang Z, Whiddon R, He Y, Li Z, et al. Quantitative Measurement of Atomic Potassium in Plumes over Burning Solid Fuels Using Infrared-Diode Laser Spectroscopy. Energy Fuels 2017;31(3):2831-7.

[14] Sorvajärvi T, DeMartini N, Rossi J, Toivonen J. In Situ Measurement Technique for Simultaneous Detection of K, KCl, and KOH Vapors Released during Combustion of Solid Biomass Fuel in a Single Particle Reactor. Appl. Spectrosc. 2014;68(2):179-84.

[15] Erbel C, Mayerhofer M, Monkhouse P, Gaderer M, Spliethoff H. Continuous in situ measurements of alkali species in the gasification of biomass. Proc. Combust. Inst. 2013;34(2):2331-8.

[16] Liu YZ, Wang ZH, Xia J, Vervisch L, Wan KD, He Y, et al. Measurement and kinetics of elemental and atomic potassium release from a burning biomass pellet. Proc. Combust. Inst. 2019;37(3):2681-8.

[17] Zhang Z-h, Song Q, Alwahabi ZT, Yao Q, Nathan GJ. Temporal release of potassium from pinewood particles during combustion. Combust. Flame 2015;162(2):496-505.

[18] Liu YZ, He Y, Wang ZH, Wan KD, Xia J, Liu JZ, et al. Multi-point LIBS measurement and kinetics modeling of sodium release from a burning Zhundong coal particle. Combust. Flame 2018;189:77-86.

[19] Fatehi H, Li ZS, Bai XS, Aldén M. Modeling of alkali metal release during biomass pyrolysis. Proc. Combust. Inst. 2017;36(2):2243-51.

[20] Van Eyk PJ, Ashman PJ, Alwahabi ZT, Nathan GJ. The release of water-bound and organic sodium from Loy Yang coal during the combustion of single particles in a flat flame. Combust. Flame 2011;158(6):1181-92.

[21] Glarborg P, Marshall P. Mechanism and modeling of the formation of gaseous alkali sulfates. Combust. Flame 2005;141(1–2):22-39.

[22] Akbar S, Schnell U, Scheffknecht G. Modelling potassium release and the effect of potassium

chloride on deposition mechanisms for coal and biomass-fired boilers. Combust. Theory Model. 2010;14(3):315-29.

[23] Garba MU, Ingham DB, Ma L, Porter RTJ, Pourkashnian M, Tan HZ, et al. Prediction of Potassium Chloride Sulfation and Its Effect on Deposition in Biomass-Fired Boilers. Energy Fuels 2012;26(11):6501-8.

[24] Hara T, Muto M, Kitano T, Kurose R, Komori S. Direct numerical simulation of a pulverized coal jet flame employing a global volatile matter reaction scheme based on detailed reaction mechanism. Combust. Flame 2015;162(12):4391-407.

[25] Muto M, Yuasa K, Kurose R. Numerical simulation of ignition in pulverized coal combustion with detailed chemical reaction mechanism. Fuel 2017;190:136-44.

[26] Wan KD, Vervisch L, Xia J, Domingo P, Wang ZH, Liu YZ, et al. Alkali metal emissions in an early-stage pulverized-coal flame: DNS analysis of reacting layers and chemistry tabulation. Proc. Combust. Inst. 2019;37(3):2791-9.

[27] Yamamoto K, Murota T, Okazaki T, Taniguchi M. Large eddy simulation of a pulverized coal jet flame ignited by a preheated gas flow. Proc. Combust. Inst. 2011;33(2):1771-8.

[28] Franchetti BM, Cavallo Marincola F, Navarro-Martinez S, Kempf AM. Large eddy simulation of a pulverised coal jet flame. Proc. Combust. Inst. 2013;34(2):2419-26.

[29] Rabaçal M, Franchetti BM, Marincola FC, Proch F, Costa M, Hasse C, et al. Large Eddy Simulation of coal combustion in a large-scale laboratory furnace. Proc. Combust. Inst. 2015;35(3):3609-17.

[30] Wan KD, Xia J, Wang ZH, Wrobel LC, Cen KF. Online-CPD-coupled large-eddy simulation of pulverized-coal pyrolysis in a hot turbulent nitrogen jet. Combust. Sci. Technol. 2017;189(1):103-31.

[31] Wen X, Luo Y, Luo K, Jin H, Fan J. LES of pulverized coal combustion with a multi-regime flamelet model. Fuel 2017;188:661-71.

[32] Rieth M, Clements AG, Rabaçal M, Proch F, Stein OT, Kempf AM. Flamelet LES modeling of coal combustion with detailed devolatilization by directly coupled CPD. Proc. Combust. Inst. 2017;36(2):2181-9.

[33] Wan KD, Xia J, Wang ZH, Pourkashanian M, Cen KF. Large-eddy Simulation of Pilot-assisted Pulverized-coal Combustion in a Weakly Turbulent Jet. Flow Turbul. Combust. 2017;99(2):531-50.

[34] Wan KD, Xia J, Vervisch L, Liu YZ, Wang ZH, Cen KF. Modelling alkali metal emissions in large-eddy simulation of a preheated pulverised-coal turbulent jet flame using tabulated chemistry. Combust. Theory Model. 2018;22(2):203-36.

[35] Hindiyarti L, Frandsen F, Livbjerg H, Glarborg P, Marshall P. An exploratory study of alkali sulfate aerosol formation during biomass combustion. Fuel 2008;87(8–9):1591-600.

[36] Li B, Sun Z, Li Z, Aldén M, Jakobsen JG, Hansen S, et al. Post-flame gas-phase sulfation of potassium chloride. Combust. Flame 2013;160(5):959-69.

[37] Kazakov A, Frenklach M. Reduced reaction sets based on GRI-Mech 1.2. 1994. (http://www.me.berkeley.edu/drm/).

[38] Sheng CD, Azevedo JLT. Modeling biomass devolatilization using the chemical percolation devolatilization model for the main components. Proc. Combust. Inst. 2002;29:407-14.

[39] Wan KD, Wang ZH, He Y, Xia J, Zhou ZJ, Zhou JH, et al. Experimental and modeling study of pyrolysis of coal, biomass and blended coal–biomass particles. Fuel 2015;139:356-64.

[40] Wang ZH, Wan KD, Xia J, He Y, Liu YZ, Liu JZ. Pyrolysis Characteristics of Coal, Biomass, and Coal–Biomass Blends under High Heating Rate Conditions: Effects of Particle Diameter, Fuel Type, and Mixing Conditions. Energy Fuels 2015;29(8):5036-46.

[41] Takuwa T, Naruse I. Emission control of sodium compounds and their formation mechanisms during coal combustion. Proc. Combust. Inst. 2007;31 II:2863-70.

[42] Goodwin DG, Moffat HK, Speth RL. Cantera: An object-oriented software toolkit for chemical kinetics, thermodynamics, and transport processes. 2017. (http://www.cantera.org). Version 2.3.0.

[43] Ma L, Jones JM, Pourkashanian M, Williams A. Modelling the combustion of pulverized biomass in an industrial combustion test furnace. Fuel 2007;86(12–13):1959-65.

[44] Li J, Biagini E, Yang W, Tognotti L, Blasiak W. Flame characteristics of pulverized torrefied-biomass combusted with high-temperature air. Combust. Flame 2013;160(11):2585-94.

[45] Wan KD, Wang ZH, Xia J, Vervisch L, Domingo P, Lv Y, et al. Numerical study of HCl and SO2 impact on sodium emissions in pulverized-coal flames. Fuel 2019;250:315-26.

[46] Knappstein R, Kuenne G, Ketelheun A, Köser J, Becker L, Heuer S, et al. Devolatilization and volatiles reaction of individual coal particles in the context of FGM tabulated chemistry. Combust. Flame 2016;169:72-84.

[47] Miller RS, Bellan J. Direct numerical simulation of a confined three-dimensional gas mixing layer with one evaporating hydrocarbon-droplet-laden stream. J. Fluid Mech. 1999;384:293-338.

[48] Ranz WE, Marshall WR. Evaporation from drops. Chem. Eng. Prog. 1952;48(3):141-6.

[49] Chandrasekhar S. Radiative transfer. New York: Dover Publications; 1960.

[50] Smith TF, Shen ZF, Friedman JN. Evaluation of Coefficients for the Weighted Sum of Gray Gases Model. J. Heat Transfer 1982;104(4):602-8.

[51] Badzioch S, Hawksley PGW. Kinetics of thermal decomposition of pulverized coal particles. Ind. Eng. Chem. Proc. Des. Dev. 1970;9(4):521-30.

[52] Pierce CD, Moin P. Progress-variable approach for large-eddy simulation of non-premixed

turbulent combustion. J. Fluid Mech. 2004;504:73-97.

[53] Desjardins O, Blanquart G, Balarac G, Pitsch H. High order conservative finite difference scheme for variable density low Mach number turbulent flows. J. Comput. Phys. 2008;227(15):7125-59.

[54] Domingo P, Vervisch L, Réveillon J. DNS analysis of partially premixed combustion in spray and gaseous turbulent flame-bases stabilized in hot air. Combust. Flame 2005;140(3):172-95.

[55] Li S, Zheng Y, Zhu M, Martinez DM, Jiang X. Large-eddy simulation of flow and combustion dynamics in a lean partially premixed swirling combustor. Journal of the Energy Institute 2017;90(1):120-31.

[56] Reveillon J, Vervisch L. Analysis of weakly turbulent dilute-spray flames and spray combustion regimes. J. Fluid Mech. 2005;537:317-47.

[57] Ekvall T, Andersson K, Leffler T, Berg M. K–Cl–S chemistry in air and oxy-combustion atmospheres. Proc. Combust. Inst. 2017;36(3):4011-8.

Figure captions

Figure 1. Schematic diagram of computational configuration. Periodic boundary conditions in all directions

Figure 2. Potassium species distribution versus distance along the 1D premixed volatile flame at equivalence ratio ϕ = 0.5 (a), ϕ = 1.0 (b) and ϕ = 2.0 (c). The heat release zone is zoomed in and shown on the left side while the overall flame is shown on the right side.

Figure 3. Comparison of potassium species distribution versus distance along the 1D premixed volatile flame between Case A (the baseline case), Case B (HCl replaced by N_2), Case C (SO_2 replaced by N_2) and Case D (both HCl and SO_2 replaced by N_2) at equivalence ratio ϕ = 0.5 (a), ϕ = 1.0 (b) and ϕ = 2.0 (c).

Figure 4. Comparison of potassium species distribution in the mixture fraction space of the 1D diffusion volatile flame among Case E (the baseline case), Case F (HCl replaced by N_2), Case G (SO_2 replaced by N_2) and Case H (both HCl and SO_2 replaced by N_2).

Figure 5. Time evolutions of instantaneous distributions of the (a) gas temperature and particle burnout, (b) OH mass fraction, (c) K mass fraction, (d) KOH mass fraction and (e) flame index and particle temperature.

Figure 6. Instantaneous distributions of all the twelve potassium species at t = 20 ms. The isoline of ϕ = 1 is superimposed.

Figure 7. Scatter plots of instantaneous mass fractions of K, KCl, KOH, $KHSO_4$, K_2SO_4 and $K_2O_2H_2$ against Z at t = 20 ms. Blue solid line and red dash line are the potassium profiles obtained from 1D counterflow diffusion flames, corresponding to the lowest (21 s^{-1}) and highest strain rates (8556 s^{-1}).

Figure 8. Time evolutions of the mean mass fractions of OH, HCl, SO_2 and Z_{vol} averaged over the 2D computational domain.

Figure 9. Time evolutions of the mean mass fractions of K, KOH, KCl, $KHSO_4$, K_2SO_4 and K_2Cl_2, and the mean gas temperature.

Figure 10. Major pathways of potassium transformation during pulverized-biomass combustion.

Figure 11. Comparison of time evolutions of the mean mass fractions of potassium species among Case J (the baseline case), Case K (HCl replaced by N_2), Case L (SO_2 replaced by N_2) and Case M (both HCl and SO_2 replaced by N_2).

Color figures can be used for the online PDF version and the gray style for hardcopy reproduction.